Structural Characterization of Low-Sr-Doped Hydroxyapatite Obtained by Solid-State Synthesis

Article *in* Crystals · January 2023

DOI: 10.3390/cryst13010117

crystals

MDPI

Article

Structural Characterization of Low-Sr-Doped Hydroxyapatite Obtained by Solid-State Synthesis

Francesco Baldassarre [1], Angela Altomare [1], Ernesto Mesto [2], Maria Lacalamita [2], Bujar Dida [3], Altin Mele [4,5], Elvira Maria Bauer [6], Massimo Puzone [7], Emanuela Tempesta [8], Davide Capelli [9], Dritan Siliqi [1,*] and Francesco Capitelli [9,*]

1 Institute of Crystallography (IC), National Research Council (CNR), Via G. Amendola, 122/O, 70126 Bari, Italy
2 Department of Earth and Environmental Sciences, University of Bari Aldo Moro, Via E. Orabona 4, 70125 Bari, Italy
3 Department of Chemistry, Faculty of Mathematic Engineering & Physical Engineering, Polytechnic University of Tirana, 1001 Tirana, Albania
4 Ivodent Academy, Center of Techniques Studies, Rruga Prokop Myzeqari, 10, 1016 Tirana, Albania
5 Department of Chemistry, Faculty of Natural Sciences, University of Tirana, Bulevardi Zog I, 25/1, 1001 Tirana, Albania
6 Institute of Structure of Matter (ISM), National Research Council (CNR), Via Salaria Km 29.300, 00016 Monterotondo, Italy
7 ENEA Trisaia Research Centre, S.S. 106 Jonica Km 419.500, 75026 Rotondella, Italy
8 Institute of Environmental Geology and Geoengineering (IGAG), National Research Council (CNR), Via Salaria Km 29.300, 00016 Monterotondo, Italy
9 Institute of Crystallography (IC), National Research Council (CNR), Via Salaria Km 29.300, 00016 Monterotondo, Italy
* Correspondence: dritan.siliqi@ic.cnr.it (D.S.); francesco.capitelli@ic.cnr.it (F.C.); Tel.: +39-080-5929164 (D.S.); +39-06-90672616 (F.C.)

Abstract: Strontium-substituted $Ca_{10}(PO_4)_6(OH)_2$ hydroxyapatite (HAp) powders, with Sr wt% concentrations of 2.5, 5.6 and 10%, were prepared by a solid-state synthesis method. The chemical composition of the samples was accurately evaluated by using inductively coupled plasma (ICP) spectroscopy. The morphology of the samples was analyzed via optical microscopy, while structural characterization was achieved through powder X-ray diffraction (PXRD) and infrared (FTIR) and Raman spectroscopy. The PXRD structural characterization showed the presence of the Sr dopant in the Ca1 structural site for HAp with a lower Sr concentration and in the Ca2 site for the sample with a higher Sr concentration. FTIR and Raman spectra showed slight band shifts and minor modifications of the (PO_4) bands with increasing the Sr doping rate.

Keywords: hydroxyapatite; strontium; solid-state synthesis; PXRD; FTIR; Raman

Citation: Baldassarre, F.; Altomare, A.; Mesto, E.; Lacalamita, M.; Dida, B.; Mele, A.; Bauer, E.M.; Puzone, M.; Tempesta, E.; Capelli, D.; et al. Structural Characterization of Low-Sr-Doped Hydroxyapatite Obtained by Solid-State Synthesis. *Crystals* **2023**, *13*, 117. https://doi.org/10.3390/cryst13010117

Academic Editors: Waldemar Maniukiewicz and Changquan Calvin Sun

Received: 16 December 2022
Accepted: 4 January 2023
Published: 9 January 2023

1. Introduction

Hydroxyapatite $Ca_{10}(PO_4)_6(OH)_2$ (HAp) is a calcium phosphate phase widely investigated in materials science owing to its interesting properties of biocompatibility, bioactivity and osteoconductivity with human biosystems, mainly due to its analogy with the mineral components of hard tissue, such as bones and teeth [1]. HAp, which naturally crystallizes predominantly in the hexagonal space group $P6_3/m$, is well known for the high flexibility of its structure [2], allowing cationic substitutions in Ca^{2+} sites, including monovalent (Na^+, K^+, etc.), bivalent (e.g., Ba^{2+}, Mg^{2+}, and Fe^{2+}) and trivalent (e.g., Al^{3+}, Ga^{3+}, and Bi^{3+}) cations; anionic substitutions in either phosphate or hydroxyl positions, with HPO_4 and CO_3 replacing the phosphate group or As and V replacing P; and halogen substitutions (F^- and Cl^-) in the $(OH)^-$ site [3]. This wide range of substitutions gives rise to many synthetic materials employed in several applications. We mention just a few HAp products: bioactive coating materials on titanium bone implants [4]; treatment of bone tumoral

pathologies [5]; maxillofacial applications to support bone growth and remodeling [6]; drug-delivery nanoparticles in personalized medicine applications [7]; anti-mycotic agents [8]. HAp, in which rare earth cations (*RE*) partially replace Ca^{2+} ions, shows significant luminescent properties [9,10] and results in being an excellent material compatible with living tissues [11]. Moreover, optical properties have been recently exploited for another class of calcium phosphates, i.e., β-tricalcium phosphate $Ca_3(PO_4)_2$ (β-TCP), doped with different *RE* cations, which are *RE* from La (Z = 57) to Lu (Z = 71) [12–14].

In the last few years, there has been a rising interest in the study of strontium-substituted hydroxyapatites. Strontium is typically associated with beneficial effects on bone tissue metabolism and osteoporosis treatment [15], although in some particular cases, i.e., in the treatment of postmenopausal osteoporosis, the occurrence of cardiovascular side effects were observed [16]; mechanisms of distribution of strontium in bone were reviewed by [17]. Analogously to bone applications, Sr-HAps are largely applied for teeth repair and cure. For example, they are employed in cement pastes for enhancing dentin remineralization [18], and in general, they are studied for their antibacterial properties [19]. Such biocements are often made by a biphasic calcium phosphate combination of HAp with β-TCP, given that it was observed that the addition of β-TCP enhances the poor mechanical properties of synthetical hydroxyapatite [20]. The applications of Sr-HAp in oral care products are also worthy of mention, such as tooth whitening, oral biofilm and toothpaste [21], while the substitution of Sr in Ag/Sr-HA nanoparticles can effectively alleviate the negative effects of Ag and enhance the biological activity of HAp [22]. In addition, the biological activity of Sr-substituted HAps coated on different scaffolds, e.g., magnesium alloys [23], titanium components [24] and poly(l-lactic acid) (PLLA) [25], has been highlighted, and the HAp biocompatibility has been improved for possible clinical applications. From a structural point of view, Sr^{2+} has been shown to enter into both Ca^{2+} cationic sites of HAp (nine- and seven-coordinated) due to the non-negligible ionic radius difference (Ca^{2+} = 1.00 Å, Sr^{2+} = 1.18 Å), with a preference for the Ca1 site at low Sr concentration and for the Ca2 site at high Sr concentration (5% at.) [26]; the presence of Sr^{2+} results in a general perturbation of the lattice, increasing cell parameters and modifying the mean size of crystal domains [27]. Lastly, about the different synthesis methods for hydroxyapatite compounds, in a previous work by us, we have observed how the degree of HAp crystallinity increased with solid-state reactions unlike wet chemistry methods [9].

The aim of the present work is to synthesize low-Sr-content HAp powders (dopant wt% concentrations of 2.5, 5.6 and 10%) and to provide an extensive multimethodological characterization based on morphological investigation via optical microscopy, chemical investigation via inductively coupled plasma (ICP) spectroscopy and structural arrangement by powder X-ray diffraction (PXRD), completed by Rietveld refinement, Fourier transform infrared (FTIR) and Raman vibrational spectroscopies. This paper contributes to effectively clarifying studies related to the structural characterization of HAps to enable their possible advanced applications.

2. Experimental

A solid-state reaction process was carried out for synthesizing a single phase of pure hydroxyapatite (HAp) and strontium-doped hydroxyapatite (Sr-HAp). A mix of homogeneous and stoichiometric quantities of calcium and phosphorous powders as precursors was used in pestle and mortar; HAp powder was prepared by mixing the compositions of the calcium and phosphorous at a molar ratio 1.67. A mixture of powders of $CaCO_3$ (MW = 100,089 g/mol, 40.04% Ca), $CaHPO_4$ (MW = 136,082, 22.76% P) and $SrCO_3$ (MW = 147.63, 59.35% Sr) was pressed uniaxially into pellets 2 mm thick and 13 mm in diameter under a load of 1.75 t for 40 s. All chemicals used were purchased from Sigma–Aldrich, St Louis, MO, USA, with a purity higher than 98%. Finally, the pellets were sintered at 1250 °C for 12 h in a Nabertherm programmable furnace to enhance the interfacial bonding and the rate of diffusion of ions and crystallize the product. Heating rates of 20 °C/min (20–200 °C), 13 °C/min (200–1250 °C) and 12 h at 1250 °C and a cooling

rate to room temperature of 5 °C/min were adopted. The samples, with theoretical Sr weight percentages of 0 (i.e., pure HAp), 2.5, 5.6 and 10%, were relabeled all along the text as Dop0, Dop1, Dop2 and Dop3, respectively. Reactions achieved for Dop0 synthesis are as follows:

$$6CaHPO_4 + 4CaCO_3 = Ca_{10}(PO_4)_6(OH)_2 + 4CO_2 + 2H_2O \quad (1)$$

Reactions achieved for Dop1–3 syntheses are as follows:

$$6CaHPO_4 + (4 - x)CaCO_3 + xSrCO_3 = Ca_{10-x}Sr_x(PO_4)_6(OH)_2 + 2H_2O + 4CO_2 \quad (2)$$

Accurate chemical analysis performed using inductively coupled plasma–optical emission spectrometry ICP-OES (PerkinElmer OPTIMA 2000™ DV, Co. Ltd., Shelton, CT, USA) provided total concentrations of Ca, P and (for Dop1–3) Sr ions in the powder samples, previously subject to acid dissolution (see below). The samples, after drying, were in the weight range of 100~110 mg and were dissolved in 5 mL of 65% ($v \cdot v^{-1}$) nitric acid and ultrapure water (up to 100 mL) for Dop0 and Dop1 samples and 5 mL of 65% ($v \cdot v^{-1}$) nitric acid with 3 mL of aqua regia and ultrapure water (up to 100 mL) for Dop2 and Dop3 samples. Aliquots of each of these solutions were diluted and brought to volume in a 100 mL volumetric flask containing the internal standard (1 $mg \cdot kg^{-1}$ of yttrium) in 3% ($v \cdot v^{-1}$) nitric acid or aqua regia. The calibration was checked using the external standard method with multielement (Ca, P and Sr) solutions ranging from 0.01 to 10 $mg \cdot L^{-1}$ in a 3% ($v \cdot v^{-1}$) nitric acid aqueous solution (for Dop0 and Dop1) or 3% ($v \cdot v^{-1}$) aqua regia (for Dop2 and Dop3) with correlation coefficient $R^2 > 0.9999$ and RSD < 5%. All samples were analyzed in triplicate. ICP-OES results are shown in Table 1.

Table 1. Weight percentages (wt%) of Ca, Sr and P and (Ca + Sr)/P molar ratios for the solid-state-synthesized HAp samples, obtained by ICP-OES.

Sample/Element	Ca	P	Sr	(Ca + Sr)/P
	wt%	wt%	wt%	molar ratio
Dop0	36.18	16.87	0.00	1.66
Dop1	36.86	18.13	2.36	1.62
Dop2	29.94	15.00	4.17	1.64
Dop3	30.10	16.50	8.26	1.59

Optical microscopy: morphological observations on all HAp samples were carried out using Morphologi G3 Malvern Panalytical (Malvern Instrument Ltd., Enigma Business Park, Groevewood Road, Malvern, Worcestershire, UK), equipped for the measurement of particle size and particle shape from 0.5 μm to several millimeters. The optical system accounts for a system of an analyzer and polarizators, which can be manually integrated within the optical circuit. Scan mode is realized through piezoelectric motors which assure the x-y-z movements with an accuracy better than 1 μm and repeatability at the level of 1 μm. Particle size distribution analysis was performed through the dedicated software Morphologi G3 (User manual, issue 5, version MAN0410).

PXRD data were collected at room temperature by using an automated Rigaku RINT2500 diffractometer (50 KV, 200 mA in Debye–Scherrer geometry) equipped with the silicon strip Rigaku D/teX Ultra detector. An asymmetric Johansson Ge (111) crystal was used to select the monochromatic Cu Kα_1 radiation (λ = 1.54056 Å). The main acquisition parameters are reported in Table 2. The angular range of 8–120° (2θ) (10–100° for the undoped HAp sample) was scanned with a step size of 0.02° (2θ) and counting time of 4 s/step. Measurements were executed in transmission mode by introducing the sample within a special glass capillary with a 0.5 mm internal diameter and mounted on the axis of the goniometer. A capillary spinner was used during measurements to reduce the effects of the preferred orientation of crystallites. The determination of the unit cell parameters, the identification of the space group, the structure solution and the model refinement via the Rietveld method [28] were carried out by the EXPO2013 software [29], a package able

to automatically execute the full pathway of the powder solution process. In particular, the indexation of powder diffraction patterns was obtained through the N-TREOR09 software [30] integrated into the EXPO2013 suite. Qualitative analysis of XRD spectra was executed through QUALX2.0 software [31] using the commercial PDF-2 database [32] and the free POW_COD database [31]. Further details of the crystal structure investigations may be obtained from the joint CCDC/FIZ Karlsruhe online 2213306 (Dop0), 2213310 (Dop1), 2213304 (Dop2) and 2213308 (Dop3).

Table 2. Acquisition and structure refinement parameters for HAp samples. FMLS: Full-Matrix Least Square.

	Dop0	**Dop1**	**Dop2**	**Dop3**
Ref. formula	$Ca_{10}(PO_4)_6(OH)_2$	$Ca_{9.98}Sr_{0.02}(PO_4)_6(OH)_2$	$Ca_{9.96}Sr_{0.04}(PO_4)_6(OH)_2$	$Ca_{9.84}Sr_{0.16}(PO_4)_6(OH)_2$
Formula wt.	1004.61	1005.98	1006.38	1019.71
Color	Colorless	Colorless	Colorless	Colorless
T (*K*)	293	293	293	293
λ (Å)	1.54056	1.54056	1.54056	1.54056
2θ; step (°)	10–100, 0.02	8–120, 0.02	8–120, 0.02	8–120, 0.02
Crystal system	Hexagonal	Hexagonal	Hexagonal	Hexagonal
Space group	$P6_3/m$	$P6_3/m$	$P6_3/m$	$P6_3/m$
$a = b$ (Å)	9.41614(14)	9.42402(6)	9.42265(2)	9.44904(14)
c (Å)	6.8816(2)	6.89026(10)	6.89277(6)	6.9150(2)
V (Å^3)	528.40(2)	529.96(1)	529.99(1)	534.69(2)
Z; $\rho_{calc.}$ (Mg·m^{-3})	1; 3.107	1; 3.152	1; 3.153	1; 3.094
Refinement	FMLS	FMLS	FMLS	FMLS
Bragg refl.	213	291	291	291
R_p; R_{wp}; R_{exp} (%)	4.79; 8.04; 4.36	3.14; 5.17, 4.91	4.12; 6.58; 5.07	3.52; 5.28; 4.72

Fourier-transformed infrared (FTIR) spectra in the spectral range of 400–4000 cm^{-1} (resolution 4 cm^{-1}) were registered on a Shimadzu Prestige-21 FTIR instrument (Shimadzu Scientific Instruments, 7102 Riverwood Drive, Columbia, MD, USA) equipped with an attenuated total reflectance (ATR) diamond crystal accessory (Specac Golden Gate). The spectral resolution was <1 cm^{-1}.

Micro-Raman spectra were acquired by means of a LabRAM HR Evolution Horiba (Horiba Advanced Techno, 2 Miyanohigashi-cho, Kisshoin 601–8551 Minami-ku, Kyoto, Japan) spectrometer equipped with a binocular Olympus microscope, a He-Ne laser (632 nm), an ultra-low frequency (ULF) filter, 600 and 1800 g/mm gratings and a Peltier-cooled CCD detector. Spectra were collected in the 300–1200 and 3500–3700 cm^{-1} ranges on pressed powders of the HAp samples using a 100x objective and an exposure time of 120 s and averaging two repeated acquisitions. Spectra were calibrated using the 520.5 cm^{-1} line of a silicon wafer.

3. Results and Discussion

3.1. Morphological Investigation

Optical microscopy investigation of pure and Sr-doped HAp samples showed the presence of grains with irregular morphology, usually subspherical (Figure 1a–d) and in some cases up to prismatic (Figure 1d), with sizes usually ranging from 1 to 10 μm; in rare cases, we observed larger grains over 10 and 20 μm (Figure 1b,c). The morphology of the present Sr-doped HAp samples is in good agreement with the findings reported in [33]. Moreover, a particle size distribution analysis was performed, owing to the method of 'scanning optical microscopy' (Morphologi G3, Malvern Instrument Ltd., Enigma Business Park, Groevewood Road, Malvern, Worcestershire, United Kingdom), based on the scanning of a large number of particles randomly disposed on a mount transparent to visible light. Particles are first photographed, after which the dedicated software Morphologi G3 measures the dimensions of each particle, normalizing them to a sphere ('circle equivalent'—

CE). Experimental CE diameter distribution curves of HAp samples (curves obtained from smoothing by an average of 29 readings) are reported in Figure 2. The CE distribution confirms the observed trend for particle size, with values in the range of 1–10 µm quite recurrent in the four samples. We only observed some specific features in these trends in Dop0 and Dop3 samples: Dop0 shows a higher occurrence (%) at about 3–5 µm, slightly larger than the other three samples, while the Dop3 sample shows a higher occurrence at about 5–20 µm (Figure 2). We may suppose that the increasing Sr concentration in the samples enables the particle distribution at this size range.

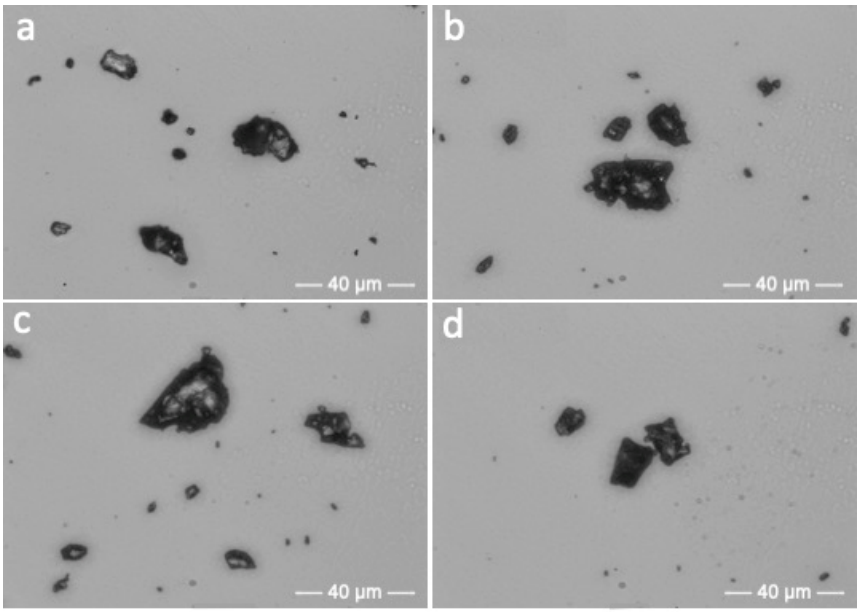

Figure 1. Optical microscopy photos of HAp samples: Dop0 (**a**); Dop1 (**b**); Dop2 (**c**); Dop3 (**d**).

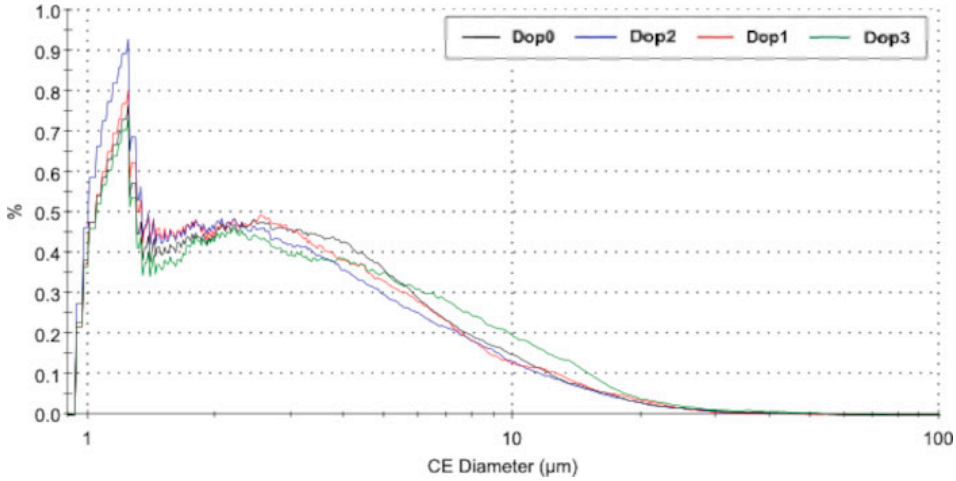

Figure 2. 'Circle equivalent' (CE) diameter distribution curves of HAp samples: the curves are obtained from the smoothing by average of 29 readings.

3.2. X-ray Diffraction Study

For all the HAp samples under investigation, the crystal structure solution steps, from indexing to structure model refinement, were achieved by using the EXPO2013 software [29]. The indexation of the powder diffraction patterns was obtained through the N-TREOR09 software [30]. Crystallite size (nm) was evaluated from the diffraction peak at 25.86° 2θ in the experimental pattern using the Scherrer equation $\tau = K\lambda/\beta\cos\theta$. Crystallinity (%) was achieved according to [34]. Results are reported in Table 3.

Table 3. Crystallite size (nm) and crystallinity (%) for HAp samples under investigation.

Parameter	Dop0	Dop1	Dop2	Dop3
Crystallite Size (nm)	136.7	128.8	127.7	96.2
Crystallinity (%)	92	91	91	86
HAp (%)	99.4	-	-	-
Sr-HAp (%)	-	99.7	99.9	60.7
CaO (%)	0.6	0.3	0.1	-
β-TCP (%)	-	-	-	39.3

All the PXRD patterns of pure and Sr-doped HAp powders consist of well-defined sharp peaks of the HAp phase (JCPDS, PDF-2, 00-089-6438) [35], with a very small amount of the CaO secondary phase (JCPDS, PDF-2, 00-078-0649) [36] in Dop0, Dop1 and Dop2 samples, as identified by the QUALX2.0 package [31] using the commercial PDF-2 database [32] and the free POW_COD database [31] and also quantified using the Rietveld method in EXPO2013 (Table 3). The sample Dop3 shows a high concentration of the β-TCP additional phase (JCPDS, PDF-2, 00-070-2065) [37]. HAp, CaO and TCP diffraction peaks appear in the observed powder PXRD spectra of the samples reported in Figure 3a,b.

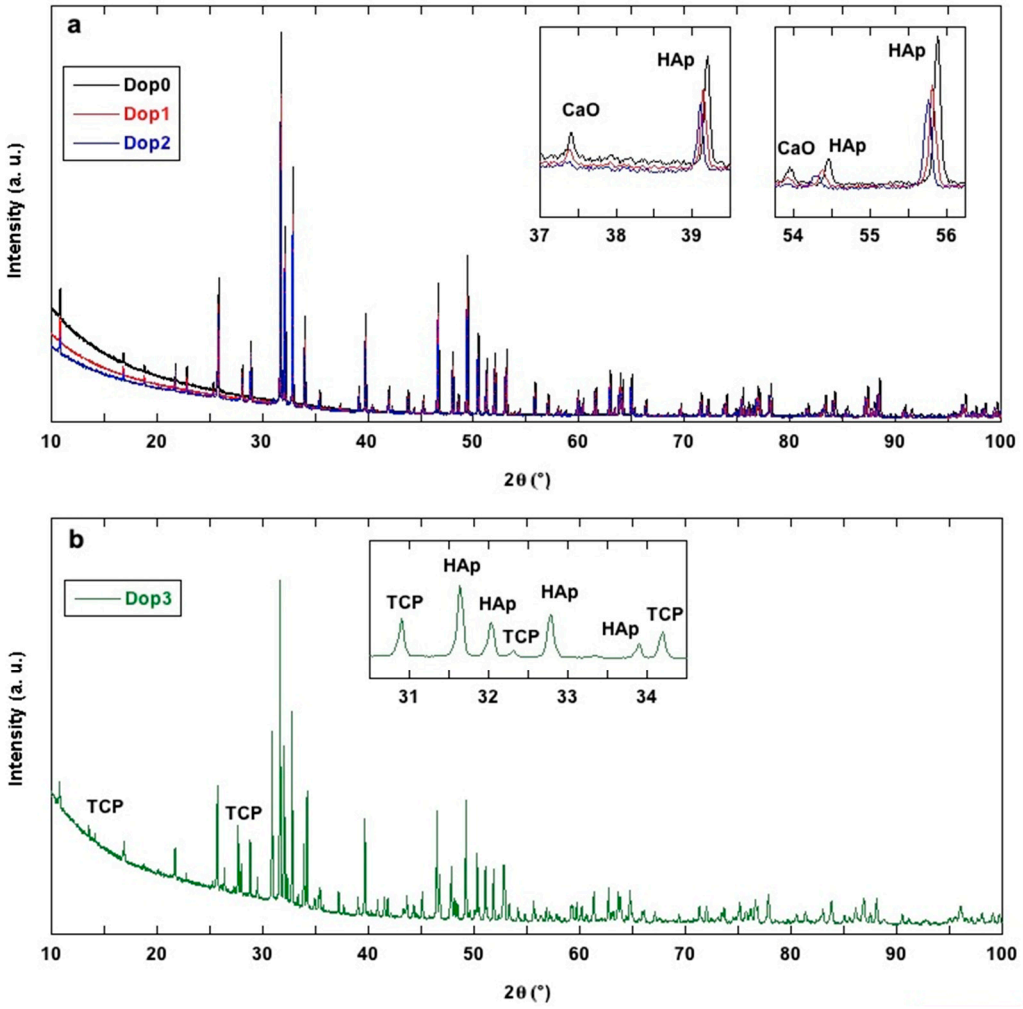

Figure 3. Observed PXRD profiles of Dop0, Dop1 and Dop3 (**a**) and Dop3 (**b**); insets: the most significant diffraction peaks corresponding to CaO (JCPDS, PDF-2, 00-078-0649) [36] (**a**) and β-TCP (JCPDS, PDF-2, 00-070-2065) [37,38], both compared with the closest HAp (JCPDS, PDF-2, 00-089-6438) [35,39] peaks.

Concerning the occurrence of β-TCP in the Dop3 sample, we have to premise that the pure HAp phase is thermally stable, but after 850 °C, at a low H_2O partial pressure, the formation of the dehydrogenated-phase $Ca_{10}(PO_4)_6O$ oxyapatite is observed by [40]. At 1050 °C, oxyapatite decomposes into TCP and $Ca_4(PO_4)_2O$ tetracalcium phosphate (depending on the water partial pressure) [40].

The occurrence of the TCP phase depends on the (Ca + Sr)/P ratio of the HAp sample: if it is lower than 1.67, the following reaction, corresponding to the decomposition (in the 375–600 °C range of temperature) of $CaHPO_4$, is reported in [41]:

$$2CaHPO_4 \rightarrow Ca_2P_2O_7 + H_2O \quad (3)$$

Similarly, in the same range of temperature, the following reaction is reported in [41]:

$$CaCO_3 + Ca_2P_2O_7 = Ca_3(PO_4)_2 + CO_2 \quad (4)$$

The first reaction did not produce any secondary phase detected by PXRD analysis in the present HAp samples even if the presence of calcium diphosphate was revealed by Raman spectroscopy, as later discussed. The second reaction can lead to the formation of β-TCP within HAp samples, as moreover observed in other high-temperature syntheses of hydroxyapatite [9,10]: a noticeable occurrence of β-TCP in HAp, as observed in the present Dop3 sample, was described from [42], characterizing biphasic (HAp + β-TCP) calcium phosphate ceramics.

With the increase in T over 1000 °C, the following reaction is conceivable:

$$Ca_{10-x}Sr_x(PO_4)_6(OH)_2 + Ca_2P_2O_7 = (4 - x)\ Ca_3(PO_4)_2 + xCa_2Sr(PO_4)_2 + H_2O\ (0 \leq x \leq 4) \quad (5)$$

These three reactions are related to the instability of calcium-deficient/nonstoichiometric HAp, showing a complex decomposition behavior depending on its initial composition. In the latter case (Equation (5)), the $Ca_2P_2O_7$ phase could subtract Ca and contribute to the massive formation of β-TCP. The isostructurality among β-TCP [38] and $Ca_2Sr(PO_4)_2$ [43] leads to difficult qualitative peak assignment in PXRD analysis. Examples of HAp/β-TCP biphasic are known in the literature, and for instance, β-TCP is added to HAp in order to counter the intrinsic brittle nature of the same hydroxyapatite: the resulting materials are promising bone substitute media [20], which, specifically when doped with strontium, become osteoporotic bone regeneration media [44].

Moreover, the Sr-Ca (partial) substitution leads also to a lattice expansion (see Table 2) due to the larger Sr atom (1.18 Å) substitution for the smaller Ca atom (1.00 Å). This substitution reflects the changes depending on the Sr content in peak positions within the spectra: a constant weak shift is generally observed toward decreasing 2θ value as a function of Sr fraction. As an example, the most intense HAp peak moves in the four samples from 2θ = 31.78° (Dop0) to 31.73 (Dop1), 31.70 (Dop2) and 31.65 (Dop3), and such gaps are mainly conserved all along the spectra as depicted in Figure 4 also for HAp peaks at 32.18° and 32.92° (values for Dop0 sample).

The lattice expansion is in agreement with the behavior of HAps doped with a higher strontium content, as reported in [45], where authors investigated a series of Sr-substituted HAps by PXRD analysis with Rietveld refinement, highlighting a linear increase in all parameters of the $P6_3/m$ HAp unit cell, i.e., a, c and V: as an example, we report the cell volume change from pure Ca-HAp to pure Sr-HAp with intermediate stages described by [45]: V = 527.5 $Å^3$ for Ca = 1.00 (Sr = 0), V = 543.8 $Å^3$ for Ca = 0.75 (Sr = 0.25), V = 562.6 $Å^3$ for Ca = 0.50 (Sr = 0.50), V = 580.3 $Å^3$ for Ca = 0.25 (Sr = 0.75) and V = 603.3 $Å^3$ for Sr = 1.00 (Ca = 0.00). The refined unit cell volume found in this work for a smaller Sr content (Table 2) fits the linear trend described by [45] (Figure 5).

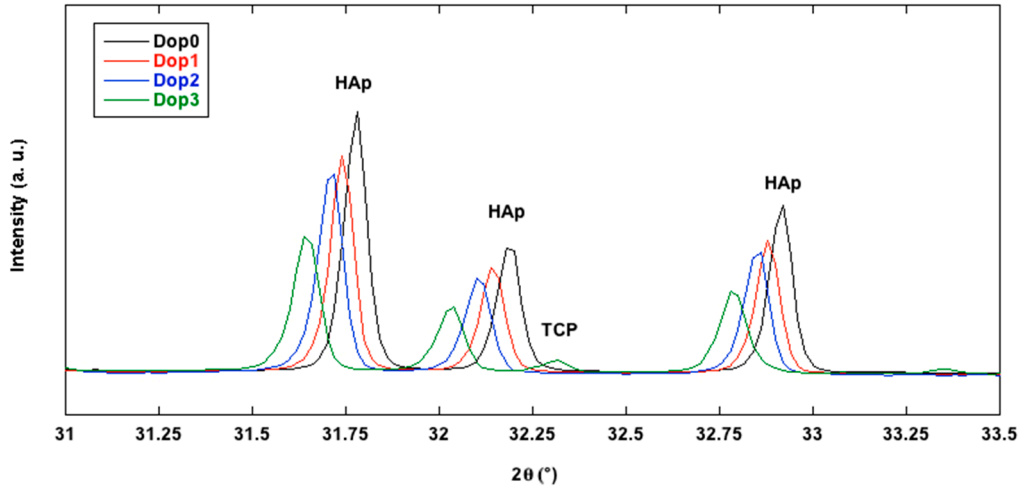

Figure 4. Variation in peak position as a function of Sr fraction for $(Ca_{1-x}Sr_x)_{10}(PO_4)_6(OH)_2$ hydroxyapatite samples.

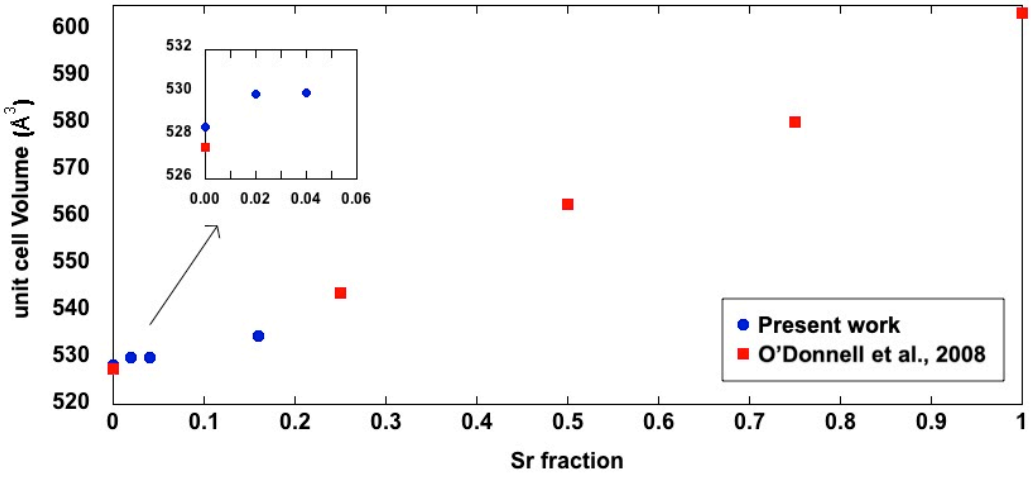

Figure 5. Variation in unit cell volume (Å^3) for $(Ca_{1-x}Sr_x)_{10}(PO_4)_6(OH)_2$ hydroxyapatite samples. Blue circles: present work. Red squares: data from O'Donnell et al., 2008 [45].

The structure solution was obtained through Direct Methods in EXPO2013 (the presence of the dopant was omitted in the solution process of Dop1–3), confirming the hexagonal $P6_3/m$ model reported in [35]. It was possible to reveal the hydrogen atom position in each of the HAp structures by Fourier analysis. For all the HAp samples, the resulting structure was submitted to the structural refinement by the Rietveld method [28], assuming both calcium sites as possible hosts of the strontium dopant and analyzing site preferences through the values of refined occupancies. Detailed crystallographic results are reported in Table 2. A common strategy was applied for all the doped samples regarding the two cationic sites: position and thermal parameters of Ca and Sr were constrained to be equal, and the sum of their occupancies was fixed according to the full site occupancy. Moreover, the thermal parameters of P and O atoms were constrained to be equal. The presence of the identified secondary phases was considered in the Rietveld refinements. Structural parameters of secondary phases were not refined (only cell parameters and the scale factor): for Dop0–2, the CaO additional phase [46], and for Dop3, the β-TCP phase [38]. A good fit between experimental and calculated profiles was obtained with a small preference of Sr on Ca1 for Dop1 and Dop2 and on Ca2 for Dop3 (see profile reliability parameters in Table 2). The main crystal structure refinement data are reported in Table 2. The agreement between the observed (blue line) and the calculated (red line) diffraction pattern is displayed, together with the background (green line) and the difference pattern plotted on the same scale (violet

line), in Figure 6 for only the Dop3 sample. The non-negligible percentage of β-TCP in Dop3 is not an obstacle to the Rietveld refinement of the Sr-doped HAp compound: it does not prevent obtaining sound refined structural parameters. Similar plots can be generated for the other two doped samples, while for pure Dop0, the Rietveld plot is similar to that reported in the literature [39].

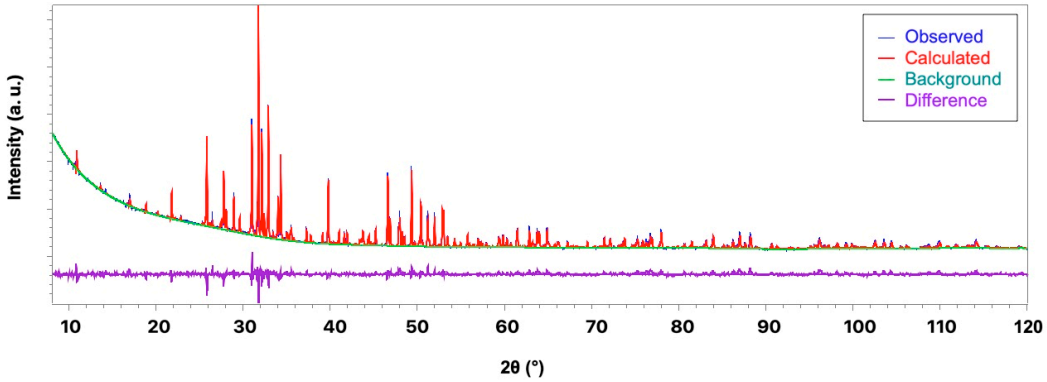

Figure 6. Rietveld plot of Dop3 sample. Observed diffraction profile (blue line), calculated profile (red line), background (green line) and difference profile (violet line).

Hydroxyapatite displays two Ca1 and Ca2 sites, engaged respectively in complex $Ca1O_9$ and $Ca2O_6(OH)$ coordinations (Figure 7). $Ca1O_9$ shows three bond distances repeated twice by symmetry, with values in the range of 2.410(4)–2.821(4) Å (Table 4). It is notable that there was a longer Ca1-O3 distance in all the samples, slightly exceeding the bonding sphere of Ca, thus providing a weak contribution to the bond valence calculation [47] for the Ca1 site (Table 4): we can deduce that, based on the refined distance values, the Ca1 site resembles a CaO_6 polyhedron, with the Ca1 ... O3 distances reviewed as weak interactions. $Ca2O_6(OH)$ resembles a distorted pentagonal bipyramid with five bonds (1xCa2-O1 and two couples of symmetry-related Ca2-O3 bonds) on the equatorial plane and vertices consisting of one O2 atom and one OH group. The Ca2-O distances are in the range of 2.323(5)–2.670(9) Å (Table 4), in good agreement with pertinent distances found in the ICSD for site Ca2 in HAp [48].

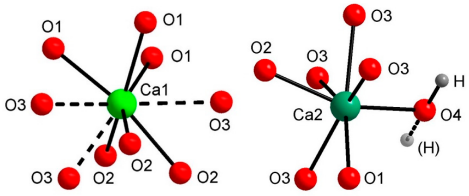

Figure 7. Coordination polyhedra at Ca1 and Ca2 sites in hydroxyapatite. Dashed lines: Ca-O interactions > 2.8 Å. O4 = (OH) site.

The (OH) group in hexagonal $P6_3/m$ hydroxyapatite lies on a special crystallographic site corresponding to a mirror plane, as observed in natural [49] and synthetic HAp [9]. In the present HAp samples, $O4_{OH}$ occupies this site, and its proton is disordered over and under the mirror (Figure 7). O-H distances derived by the Rietveld refinement are 1.18(3) Å (Dop0), 0.93(1) Å (Dop1) Å, 0.90(1) Å (Dop2) and 1.14(3) Å (Dop3), in good agreement with [50].

Phosphorous displays a regular tetrahedral coordination, typical for all inorganic orthophosphates [13,51], with bond lengths in the range of 1.562(4)–1.602(9) (Table 4); as observed in other structure solutions from powder X-ray data [52,53], they are quite long if compared with results from single-crystal X-ray diffraction [48].

Table 4. Bond distances (Å) and bond valence parameters (valence units) for pure and Sr-doped HAp samples.

Distance	Dop0	*bvp*	Dop1	*bvp*	Dop2	*bvp*	Dop3	*bvp*
3xCa1-O1	2.410(6)	*0.30*	2.414(5)	*0.30*	2.410(4)	*0.30*	2.421(6)	*0.29*
3xCa1-O2	2.419(7)	*0.30*	2.431(4)	*0.29*	2.433(7)	*0.28*	2.414(7)	*0.30*
3xCa1-O3	2.819(6)	*0.10*	2.821(4)	*0.10*	2.808(5)	*0.10*	2.819(6)	*0.10*
		2.09		***2.05***		***2.06***		***2.08***
Ca2-O1	2.647(12)	*0.16*	2.667(7)	*0.15*	2.670(9)	*0.15*	2.632(11)	*0.17*
Ca2-O2	2.327(9)	*0.38*	2.353(5)	*0.35*	2.354(7)	*0.35*	2.365(8)	*0.34*
2xCa2 O3	2.323(5)	*0.38*	2.332(3)	*0.37*	2.332(5)	*0.37*	2.322(5)	*0.38*
2xCa2 O3	2.482(8)	*0.25*	2.474(5)	*0.25*	2.490(6)	*0.24*	2.518(8)	*0.25*
$Ca2\text{-}O4_{OH}$	2.365(2)	*0.34*	2.386(2)	*0.32*	2.387(2)	*0.32*	2.377(2)	*0.33*
		2.14		***2.40***		***2.38***		***2.05***
P1-O1	1.569(12)	*1.14*	1.565(7)	*1.15*	1.573(9)	*1.12*	1.578(12)	*1.10*
P1-O2	1.602(9)	*1.04*	1.562(5)	*1.16*	1.555(7)	*1.18*	1.590(6)	*1.08*
2xP1-O3	1.566(6)	*1.15*	1.568(4)	*1.14*	1.562(4)	*1.16*	1.580(6)	*1.10*
		4.47		***4.60***		***4.63***		***4.40***

The framework of hexagonal $P6_3/m$ hydroxyapatite, whose crystal formula can be written as $[Ca1_4Ca2_6](PO_4)_6(OH)_2$, can be reviewed as a three-dimensional network made up of columns of face-sharing $Ca1O_6$ metaprisms (a polyhedron intermediate between an octahedron and a trigonal prism), corner-connected to PO_4 tetrahedra down [001]; such an environment leads to the presence of one-dimensional tunnels occupied by $[Ca2_6(OH)_2]^{10+}$ counter-ions (Figure 8). According to the bond distances reported in Table 4, the $Ca1O_6$ metaprism can be considered made by the six strongest Ca-O bond distances, not considering those over 2.8 Å. The HAp framework has an ideal stoichiometry $[Ca1_4(PO_4)_6]^{10-}$, with the hexagonal channel containing $[Ca2_6(OH)_2]^{10+}$ moieties acting as counter-ions, while the Ca1-O3 interactions concur to stabilize the framework.

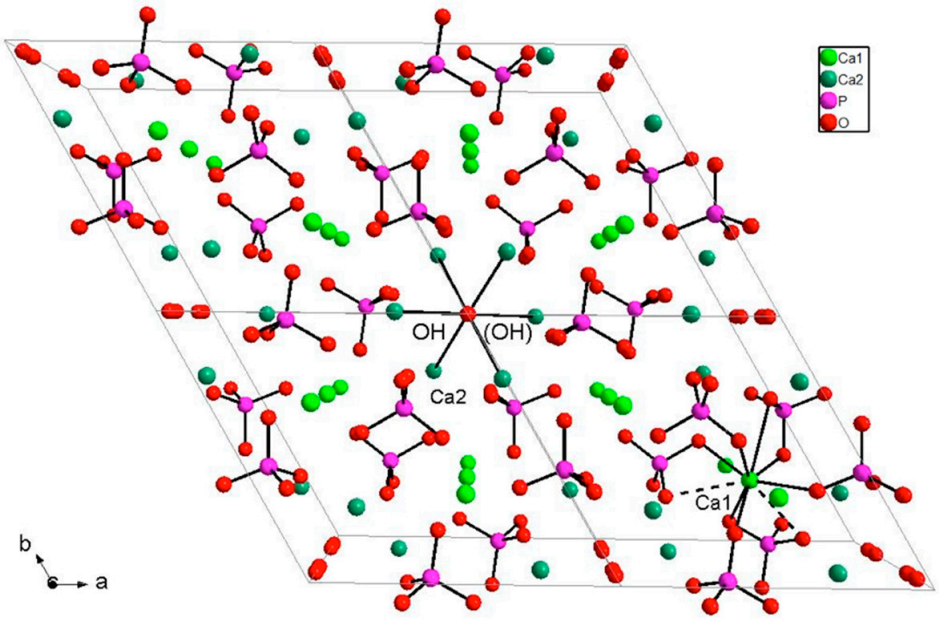

Figure 8. View of a quadruple unit cell of HAp sample, with details of $Ca1O_6$ metaprisms and $Ca2_6(OH)_2$ groups. (OH) groups correspond to O4 atoms. Ca1-O3 bonds over 2.8 Å are dashed for clarity. H atoms are not drawn for clarity.

To investigate the distribution of Sr dopant within the available sites, we examined the calculated bond valence parameters [47], testing the possible dopant localization in both Ca1 and Ca2 cationic positions: the occupancy refinements converged into the presence of the Sr cation on the Ca1 site for Dop1 and Dop2 samples, i.e., those with a lower Sr concentration, while Sr enters the Ca2 site in the Dop3 sample, which has a higher Sr concentration; both results are in agreement with the substitution mechanisms described by [26]. Refined occupancy values for the Ca1 site were Ca = 0.993(3)/Sr = 0.007(3) for Dop1 and Ca = 0.991(3)/0.009(3) for Dop2, while that for Ca2 in Dop3 was Ca = 0.973(3)/Sr = 0.027(3), in relatively good agreement with the expected values. These findings were confirmed by the calculated bond valence sum (bvs) analysis: Ca1 in the Dop1 and Dop2 doped samples and Ca2 in Dop3 display values close to the ideal value of 2.00 valence units (Table 4). The Ca2 site displays bvs values larger than 2.38 v.u. in Dop1 and Dop2, probably for packing reasons. The long P-O distances in (PO_4) tetrahedral groups lead to values of bvs for the P site that are lower than the ideal values of 5.00 v.u. The final results of the bond valence parameters analysis are given in Table 4.

3.3. FTIR and Raman Spectroscopy

FTIR and Raman spectroscopic characterizations of hydroxyapatite phases are reported in several studies [9,10,54,55]. Orthophosphate phases are usually characterized by a strong molecular character with respect to their vibrational properties so that both FTIR and Raman spectra are dominated by the internal PO_4^{3-} vibrational modes. The $(PO_4)^{3-}$ ion has four modes of vibration: symmetric stretching $\nu_1(A_1)$ at 980 cm^{-1}, symmetric bending $\nu_2(E)$ at 420 cm^{-1}, antisymmetric stretching $\nu_3(F_2)$ at 1082 cm^{-1} and antisymmetric bending $\nu_4(F_2)$ at 567 cm^{-1} [55]. In accordance with selection rules, the triply degenerate antisymmetric stretching and bending modes (F_2) are both Raman- and infrared-active, whereas the nondegenerate symmetric stretching (A_1) and the doubly degenerate symmetric bending (E) are Raman-active only. The band splitting of solid materials is usually characterized by the shift and removal of degeneracies typically due to crystal-field effects [9]. The powder FTIR transmittance spectra of undoped and Sr-doped HAp samples, collected in the 450–4000 cm^{-1} range, are reported in Figure 9; measured band positions (wavenumbers, cm^{-1}) are listed in Table 5.

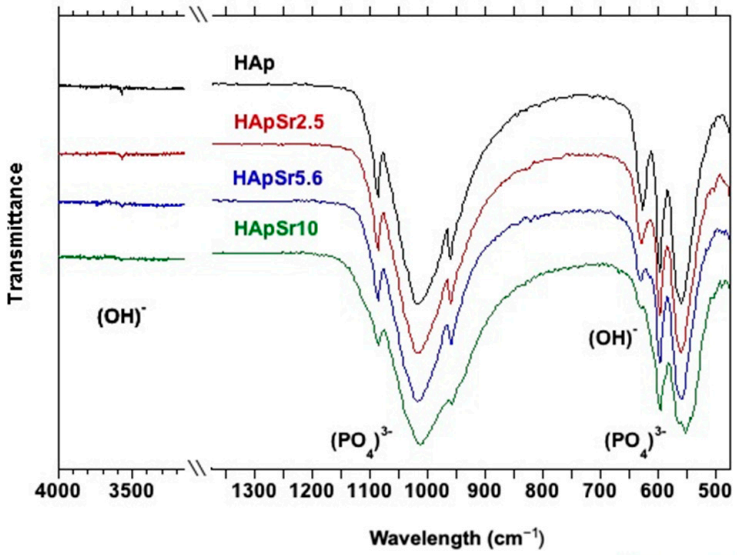

Figure 9. FTIR spectra of Sr-doped HAp samples together with undoped HAp.

Table 5. FTIR band positions (wavenumbers, cm^{-1}) and relative assignments for Sr-doped and undoped HAp samples.

Dop0	Dop1	Dop2	Dop3	Assignment
3572	3572	3570	3571	ν_s(OH)
1087	1086	1085	1083	
1020	1017	1017	1013	$\nu_3(PO_4)^{3-}$
959	957	957	955	$\nu_1(PO_4)^{3-}$
627	629	631	631	δ(OH)
597	597	597	596	
560	560	558	553	$\nu_4(PO_4)^{3-}$
472	472	471	466	$\nu_2(PO_4)^{3-}$

The analysis of the IR spectrum of pure HAp starts from the sharp peak at 3572 cm^{-1} (Table 5), which is due to the stretching mode of the $(OH)^-$ group [54]: this characteristic peak can be considered the fingerprinting of the hydroxyapatite phase in FTIR spectra; a decrease in the intensity of this peak is observed with increasing Sr concentration, as a result of the partial Sr^{2+} substitution for the Ca^{2+} ions surrounding the (OH) group, in agreement with [56]; it is also conceivable that the presence of β-TCP in the Dop3 sample contributes to lower the (OH) peak, even if no reliable presence of hydroxyl peak was observed in the pertinent FTIR spectrum.

Moreover, the spectrum of pure HAp shows an intense doublet at 1087–1020 cm^{-1} pertinent to asymmetric stretching (ν3) and a weak peak at 959 cm^{-1} (Table 5) that can be assigned to the symmetric stretching mode of the $[PO_4]^{3-}$ group [54] (Table 5). A strong peak at 627 cm^{-1} is attributed to the bending mode of the $(OH)^-$ group [9], and similar to the stretching mode at 3572 cm^{-1}, we observe a decrease in the intensity of this peak, imputable to the same substitution of Sr-Ca [56] previously observed; finally, two strong and sharp peaks at 597 and 560 cm^{-1} are attributed to the triple degenerate antisymmetric bending mode of the $[PO_4]^{3-}$ group [9] (Table 5). The sharpness of the latter three peaks, respectively, 627, 597 and 560 cm^{-1}, are considered a reliable indicator of the crystallinity of the sample [57]: it should be explained that the minor sharpness of such bands in the Dop3 sample, as stated before in the PXRD result analysis, presents the lower crystallinity among the four samples.

As a general remark, the X-ray structure refinement data described above show that the entry of Sr into the HAp structure does not modify the phosphate framework. Accordingly, no significant changes in the P-O modes are observed in the FTIR spectra except for very slight decreasing shifts in peak positions (Table 5).

Figure 10a,b show the Raman spectra collected for the undoped and Sr-HAp samples, whereas Table 6 lists the observed band positions and the related assignments. The spectra evidence the characteristic bands due to the modes of vibration of the $[PO_4]^{3-}$ groups [54]. In detail, the prominent band, centered at about 960 cm^{-1}, is associated with the symmetric stretching of the $[PO_4]^{3-}$ groups, whereas the bands observed between ~1029 and 1078 cm^{-1} are due to the $[PO_4]^{3-}$ asymmetric stretching vibrations (Table 6) (Figure 10a). Visible at lower wavenumbers are, instead, the bands at ~429 and 447 cm^{-1} due to the ν_2 $(PO_4)^{3-}$ vibrations and those between ~580 and 608 cm^{-1} due to the $(PO_4)^{3-}$ bending vibrations (Table 6). By increasing the Sr substitution in the HAp, the Raman bands associated with the vibration of the $[PO_4]^{3-}$ groups became slightly broadened due to the enhancement of the crystal structure disorder and the reduction in the crystallite size (Table 3) as revealed by the PXRD analysis and as previously reported in [27]. An additional band at 330 cm^{-1} (Figure 10a) and a strong peak at about 3574 cm^{-1} (Figure 10b) are observed in the spectra of all samples except for the Dop3 sample (Table 6). They are ascribed to Ca-OH and OH stretching modes, respectively. These peaks are absent in the Dop3 sample due to the loss of OH groups, which are required to maintain electroneutrality when Sr substitutes the Ca atoms in the apatite structure [27]. Finally, in the spectrum of

the Dop3 sample, a band at 630 cm^{-1} was observed (Table 6). It may be related to the ν_4 vibration of the β-TCP [58] as also detected by the PXRD analysis.

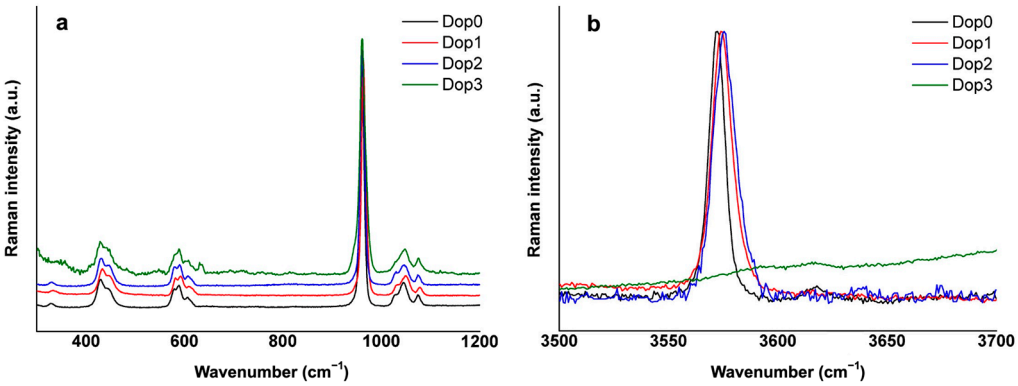

Figure 10. Raman spectra of Sr-doped HAp samples compared with the undoped HAp in 300–1200 cm^{-1} (**a**) and 3500–3700 cm^{-1} ranges (**b**).

Table 6. Raman band positions (wavenumbers, cm^{-1}) and relative assignments for Sr-doped and undoped HAp samples.

Dop0	Dop1	Dop2	Dop3	Assignment
329	330	330		ν_3(Ca-OH)
430	434	431	429	$\nu_2(PO_4)^{3-}$
445	446	447	445	
580	581	581	580	
589	593	590	589	$\nu_4(PO_4)^{3-}$
606	608	607	608	
961	963	961	958	$\nu_1(PO_4)^{3-}$
1029	1031	1030		
1044	1049	1046	1045	$\nu_3(PO_4)^{3-}$
1073	1078	1073	1072	
3572	3574	3576		ν(OH)

4. Conclusions

In this work, low-Sr-doped hydroxyapatite powders were synthesized by using a solid-state synthesis technique: the doping rates were chosen to differentiate from other works present in the literature with higher Sr concentrations. The work aims to provide a detailed structural characterization, focusing on the Sr doping effects on the crystal structures. Morphological observations showed the presence of massive fragments, with the most recurrent size under 20 microns. The PXRD characterization highlighted the high purity (i.e., absence of accessory phases) of samples with the lowest Sr concentrations (i.e., 2.5 and 5.6 wt%) and a high tricalcium phosphate concentration (ca. 40%) for the highest-Sr-concentration (10 wt%) sample; PXRD also showed an increase in unit cell parameters of the samples, consistent with the partial substitution of the smaller Ca^{2+} (1.00 Å) with the larger Sr^{2+} (1.18 Å). Rietveld refinement showed that the Sr entered the Ca1 site for samples with a lower dopant concentration and Ca2 for the sample with a higher dopant concentration. Vibrational spectroscopy, both FTIR and Raman, showed slight decreasing shifts in position as a result of the increase in the Sr dopant.

Author Contributions: F.B., D.S. and F.C. conceived and coordinated the study. F.B., D.S., D.C., B.D. and A.M. contributed to the synthesis of the hydroxyapatite; A.A. and F.B. carried out PXRD data collection, structure solution and Rietveld refinement; E.M.B. and F.C. contributed to FTIR spectroscopy; E.M. and M.L. contributed to Raman spectroscopy; E.T. contributed to optical microscopy; M.P. contributed to ICP-OES spectroscopy. All authors have read and agreed to the published version of the manuscript.

Funding: This research received no external funding.

Acknowledgments: Research developed within the activities of Bilateral Scientific Cooperation Project 2018–2019 'New nanomaterials for applications in conservation and consolidation of stony materials part of Culture Heritage in Albania' between *Consiglio Nazionale delle Ricerche* (CNR) and the Ministry of Education and Sport of the Republic of Albania (MoES). The micro-Raman spectrometer was funded by Potenziamento Strutturale PONa3_00369 "*Laboratorio per lo Sviluppo Integrato delle Scienze e delle Tecnologie dei Materiali Avanzati e per dispositivi innovativi* (SISTEMA)". D.S. acknowledges the CNCCS Consortium Project "*Collezione di Composti Chimici ed attivita di screening*". F.C. thanks Antonello Ranieri and Gaetano Campi (IC—CNR) for the helpful discussion on phosphate XRD spectra representation.

Conflicts of Interest: The authors declare no conflict of interest. The funding sponsors had no role in the design of the study; in the collection, analyses, or interpretation of data; in the writing of the manuscript, and in the decision to publish the results.

References

1. Dorozhkin, S.V. Calcium Orthophosphate Bioceramics. *Ceram. Int.* **2015**, *41*, 13913–13966. [CrossRef]
2. Hughes, J.M.; Rakovan, J. The Crystal Structure of Apatite, $Ca_5(PO_4)_3(F,OH,Cl)$. *Rev. Mineral. Geochem.* **2002**, *48*, 1–12. [CrossRef]
3. Cacciotti, I. Cationic and Anionic Substitutions in Hydroxyapatite. In *Handbook of Bioceramics and Biocomposites*; Antoniac, I.V., Ed.; Springer International Publishing: Cham, Switzerland, 2016; pp. 145–211, ISBN 978-3-319-12459-9.
4. Suchanek, W.; Yoshimura, M. Processing and Properties of Hydroxyapatite-Based Biomaterials for Use as Hard Tissue Replacement Implants. *J. Mater. Res.* **1998**, *13*, 94–117. [CrossRef]
5. Zhang, K.; Zhou, Y.; Xiao, C.; Zhao, W.; Wu, H.; Tang, J.; Li, Z.; Yu, S.; Li, X.; Min, L.; et al. Application of Hydroxyapatite Nanoparticles in Tumor-Associated Bone Segmental Defect. *Sci. Adv.* **2019**, *5*, eaax6946. [CrossRef]
6. Balamurugan, A.; Rebelo, A.H.S.; Lemos, A.F.; Rocha, J.H.G.; Ventura, J.M.G.; Ferreira, J.M.F. Suitability Evaluation of Sol–Gel Derived Si-Substituted Hydroxyapatite for Dental and Maxillofacial Applications through in Vitro Osteoblasts Response. *Dent. Mater.* **2008**, *24*, 1374–1380. [CrossRef]
7. Lara-Ochoa, S.; Ortega-Lara, W.; Guerrero-Beltrán, C.E. Hydroxyapatite Nanoparticles in Drug Delivery: Physicochemistry and Applications. *Pharmaceutics* **2021**, *13*, 1642. [CrossRef]
8. El Khouri, A.; Zegzouti, A.; Elaatmani, M.; Capitelli, F. Bismuth-Substituted Hydroxyapatite Ceramics Synthesis: Morphological, Structural, Vibrational and Dielectric Properties. *Inorg. Chem. Commun.* **2019**, *110*, 107568. [CrossRef]
9. Baldassarre, F.; Altomare, A.; Corriero, N.; Mesto, E.; Lacalamita, M.; Bruno, G.; Sacchetti, A.; Dida, B.; Karaj, D.; Ventura, G.D.; et al. Crystal Chemistry and Luminescence Properties of Eu-Doped Polycrystalline Hydroxyapatite Synthesized by Chemical Precipitation at Room Temperature. *Crystals* **2020**, *10*, 250. [CrossRef]
10. Paterlini, V.; Bettinelli, M.; Rizzi, R.; El Khouri, A.; Rossi, M.; Della Ventura, G.; Capitelli, F. Characterization and Luminescence of Eu^{3+}- and Gd^{3+}-Doped Hydroxyapatite $Ca_{10}(PO_4)_6(OH)_2$. *Crystals* **2020**, *10*, 806. [CrossRef]
11. Neacsu, I.A.; Stoica, A.E.; Vasile, B.S.; Andronescu, E. Luminescent Hydroxyapatite Doped with Rare Earth Elements for Biomedical Applications. *Nanomaterials* **2019**, *9*, 239. [CrossRef]
12. El Khouri, A.; Elaatmani, M.; Della Ventura, G.; Sodo, A.; Rizzi, R.; Rossi, M.; Capitelli, F. Synthesis, Structure Refinement and Vibrational Spectroscopy of New Rare-Earth Tricalcium Phosphates $Ca_9RE(PO_4)_7$ (RE = La, Pr, Nd, Eu, Gd, Dy, Tm, Yb). *Ceram. Int.* **2017**, *43*, 15645–15653. [CrossRef]
13. Capitelli, F.; Rossi, M.; ElKhouri, A.; Elaatmani, M.; Corriero, N.; Sodo, A.; Della Ventura, G. Synthesis, Structural Model and Vibrational Spectroscopy of Lutetium Tricalcium Phosphate $Ca_9Lu(PO_4)_7$. *J. Rare Earths* **2018**, *36*, 1162–1168. [CrossRef]
14. Rizzi, R.; Capitelli, F.; Lazoryak, B.I.; Morozov, V.A.; Piccinelli, F.; Altomare, A. A Comprehensive Study of $Ca_9Tb(PO_4)_7$ and $Ca_9Ho(PO_4)_7$ Doped β-Tricalcium Phosphates: *Ab Initio* Crystal Structure Solution, Rietveld Analysis, and Dielectric Properties. *Cryst. Growth Des.* **2021**, *21*, 2263–2276. [CrossRef]
15. Kołodziejska, B.; Stępień, N.; Kolmas, J. The Influence of Strontium on Bone Tissue Metabolism and Its Application in Osteoporosis Treatment. *Int. J. Mol. Sci.* **2021**, *22*, 6564. [CrossRef]
16. Frasnelli, M.; Cristofaro, F.; Sglavo, V.M.; Dirè, S.; Callone, E.; Ceccato, R.; Bruni, G.; Cornaglia, A.I.; Visai, L. Synthesis and Characterization of Strontium-Substituted Hydroxyapatite Nanoparticles for Bone Regeneration. *Mater. Sci. Eng. C* **2017**, *71*, 653–662. [CrossRef]
17. Marx, D.; Rahimnejad Yazdi, A.; Papini, M.; Towler, M. A Review of the Latest Insights into the Mechanism of Action of Strontium in Bone. *Bone Rep.* **2020**, *12*, 100273. [CrossRef]
18. Jayasree, R.; Kumar, T.S.S.; Mahalaxmi, S.; Abburi, S.; Rubaiya, Y.; Doble, M. Dentin Remineralizing Ability and Enhanced Antibacterial Activity of Strontium and Hydroxyl Ion Co-Releasing Radiopaque Hydroxyapatite Cement. *J. Mater. Sci. Mater. Med.* **2017**, *28*, 95. [CrossRef]
19. Kolmas, J.; Groszyk, E.; Kwiatkowska-Różycka, D. Substituted Hydroxyapatites with Antibacterial Properties. *BioMed Res. Int.* **2014**, *2014*, 1–15. [CrossRef]

20. Ebrahimi, M.; Botelho, M. Biphasic Calcium Phosphates (BCP) of Hydroxyapatite (HA) and Tricalcium Phosphate (TCP) as Bone Substitutes: Importance of Physicochemical Characterizations in Biomaterials Studies. *Data Brief* **2017**, *10*, 93–97. [CrossRef]
21. Chen, F.; Zhu, Y.-J.; Zhang, K.-H.; Wu, J.; Wang, K.-W.; Tang, Q.-L.; Mo, X.-M. Europium-Doped Amorphous Calcium Phosphate Porous Nanospheres: Preparation and Application as Luminescent Drug Carriers. *Nanoscale Res. Lett.* **2011**, *6*, 67. [CrossRef]
22. Li, Y.; Wang, W.; Han, J.; Li, Z.; Wang, Q.; Lin, X.; Ge, K.; Zhou, G. Synthesis of Silver- and Strontium-Substituted Hydroxyapatite with Combined Osteogenic and Antibacterial Activities. *Biol. Trace Elem. Res.* **2022**, *200*, 931–942. [CrossRef]
23. Gu, X.; Lin, W.; Li, D.; Guo, H.; Li, P.; Fan, Y. Degradation and Biocompatibility of a Series of Strontium Substituted Hydroxyapatite Coatings on Magnesium Alloys. *RSC Adv.* **2019**, *9*, 15013–15021. [CrossRef]
24. Nguyen, T.-D.T.; Jang, Y.-S.; Lee, M.-H.; Bae, T.-S. Effect of Strontium Doping on the Biocompatibility of Calcium Phosphate-Coated Titanium Substrates. *J. Appl. Biomater. Funct. Mater.* **2019**, *17*, 228080001982651. [CrossRef]
25. Ge, M.; Ge, K.; Gao, F.; Yan, W.; Liu, H.; Xue, L.; Jin, Y.; Ma, H.; Zhang, J. Biomimetic Mineralized Strontium-Doped Hydroxyapatite on Porous Poly(L-Lactic Acid) Scaffolds for Bone Defect Repair. *Int. J. Nanomed.* **2018**, *13*, 1707–1721. [CrossRef]
26. Terra, J.; Dourado, E.R.; Eon, J.-G.; Ellis, D.E.; Gonzalez, G.; Rossi, A.M. The Structure of Strontium-Doped Hydroxyapatite: An Experimental and Theoretical Study. *Phys. Chem. Chem. Phys.* **2009**, *11*, 568–577. [CrossRef]
27. Cheng, G.; Zhang, Y.; Yin, H.; Ruan, Y.; Sun, Y.; Lin, K. Effects of Strontium Substitution on the Structural Distortion of Hydroxyapatite by Rietveld Refinement and Raman Spectroscopy. *Ceram. Int.* **2019**, *45*, 11073–11078. [CrossRef]
28. Rietveld, H.M. A Profile Refinement Method for Nuclear and Magnetic Structures. *J. Appl. Crystallogr.* **1969**, *2*, 65–71. [CrossRef]
29. Altomare, A.; Cuocci, C.; Giacovazzo, C.; Moliterni, A.; Rizzi, R.; Corriero, N.; Falcicchio, A. *EXPO2013*: A Kit of Tools for Phasing Crystal Structures from Powder Data. *J. Appl. Crystallogr.* **2013**, *46*, 1231–1235. [CrossRef]
30. Altomare, A.; Campi, G.; Cuocci, C.; Eriksson, L.; Giacovazzo, C.; Moliterni, A.; Rizzi, R.; Werner, P.-E. Advances in Powder Diffraction Pattern Indexing: *N-TREOR09*. *J. Appl. Crystallogr.* **2009**, *42*, 768–775. [CrossRef]
31. Altomare, A.; Corriero, N.; Cuocci, C.; Falcicchio, A.; Moliterni, A.; Rizzi, R. *QUALX2.0*: A Qualitative Phase Analysis Software Using the Freely Available Database POW_COD. *J. Appl. Crystallogr.* **2015**, *48*, 598–603. [CrossRef]
32. *PDF-2 ICDD, The Powder Diffraction File*; International Center for Diffraction Data: Newton Square, PA, USA, 2003.
33. Mardziah, C.M.; Sopyan, I.; Nik Roselina, N.R.; Hyie, K.M. Effect of Calcining Temperatures on the Morphology and Crystallinity of Strontium Doped Hydroxyapatite Nanopowders. *Adv. Mater. Res.* **2013**, *772*, 325–330. [CrossRef]
34. Landi, E.; Tampieri, A.; Celotti, G.; Sprio, S. Densification Behaviour and Mechanisms of Synthetic Hydroxyapatites. *J. Eur. Ceram. Soc.* **2000**, *20*, 2377–2387. [CrossRef]
35. Wilson, R.M.; Elliott, J.C.; Dowker, S.E.P. Rietveld Refinement of the Crystallographic Structure of Human Dental Enamel Apatites. *Am. Mineral.* **1999**, *84*, 1406–1414. [CrossRef]
36. Natta, G.; Passerini, L. Soluzioni solide, isomorfismo e simmorfismo tra gli ossidi dei metalli bivalenti. Sistemi: CaO-CdO. CaO-MnO, CaO-CoO, CaO-NiO, CaO-MgO. *Gazz. Chim. Ital.* **1929**, *59*, 129–154.
37. Dickens, B.; Schroeder, L.W.; Brown, W.E. Crystallographic Studies of the Role of Mg as a Stabilizing Impurity in β-$Ca_3(PO_4)_2$. The Crystal Structure of Pureβ-$Ca_3(PO_4)_2$. *J. Solid State Chem.* **1974**, *10*, 232–248. [CrossRef]
38. Yashima, M.; Sakai, A.; Kamiyama, T.; Hoshikawa, A. Crystal Structure Analysis of β-Tricalcium Phosphate $Ca_3(PO_4)_2$ by Neutron Powder Diffraction. *J. Solid State Chem.* **2003**, *175*, 272–277. [CrossRef]
39. Okazaki, M.; Taira, M.; Takahashi, J. Rietveld Analysis and Fourier Maps of Hydroxyapatite. *Biomaterials* **1997**, *18*, 795–799. [CrossRef]
40. Trombe, J.C.; Montel, G. Some Features of the Incorporation of Oxygen in Different Oxidation States in the Apatitic Lattice—I on the Existence of Calcium and Strontium Oxyapatites. *J. Inorg. Nucl. Chem.* **1978**, *40*, 15–21. [CrossRef]
41. Rey, C.; Combes, C.; Drouet, C.; Grossin, D. Bioactive Ceramics: Physical Chemistry. In *Comprehensive Biomaterials*; Elsevier: Amsterdam, The Netherlands, 2011; pp. 187–221, ISBN 978-0-08-055294-1.
42. Obadia, L.; Rouillon, T.; Bujoli, B.; Daculsi, G.; Bouler, J.M. Calcium-Deficient Apatite Synthesized by Ammonia Hydrolysis of Dicalcium Phosphate Dihydrate: Influence of Temperature, Time, and Pressure. *J. Biomed. Mater. Res.* **2007**, *80*, 32–42. [CrossRef]
43. Belik, A.A.; Izumi, F.; Stefanovich, S.Y.; Malakho, A.P.; Lazoryak, B.I.; Leonidov, I.A.; Leonidova, O.N.; Davydov, S.A. Polar and Centrosymmetric Phases in Solid Solutions $Ca_{3-x}Sr_x(PO_4)_2$ ($0 \leq x \leq 16/7$). *Chem. Mater.* **2002**, *14*, 3197–3205. [CrossRef]
44. Zarins, J.; Pilmane, M.; Sidhoma, E.; Salma, I.; Locs, J. The Role of Strontium Enriched Hydroxyapatite and Tricalcium Phosphate Biomaterials in Osteoporotic Bone Regeneration. *Symmetry* **2019**, *11*, 229. [CrossRef]
45. O'Donnell, M.D.; Fredholm, Y.; De Rouffignac, A.; Hill, R.G. Structural Analysis of a Series of Strontium-Substituted Apatites. *Acta Biomater.* **2008**, *4*, 1455–1464. [CrossRef]
46. Verbraeken, M.C.; Suard, E.; Irvine, J.T.S. Structural and Electrical Properties of Calcium and Strontium Hydrides. *J. Mater. Chem.* **2009**, *19*, 2766. [CrossRef]
47. Brown, I.D.; Altermatt, D. Bond-Valence Parameters Obtained from a Systematic Analysis of the Inorganic Crystal Structure Database. *Acta Crystallogr. Sect. B Struct. Sci.* **1985**, *41*, 244–247. [CrossRef]
48. *Inorganic Crystal Structure Database (ICSD), Version 2018–2*; Fachinformationszentrum: Karlsruhe, Germany, 2018.
49. Rossi, M.; Ghiara, M.R.; Chita, G.; Capitelli, F. Crystal-Chemical and Structural Characterization of Fluorapatites in Ejecta from Somma-Vesuvius Volcanic Complex. *Am. Mineral.* **2011**, *96*, 1828–1837. [CrossRef]
50. Chiari, G.; Ferraris, G. The Water Molecule in Crystalline Hydrates Studied by Neutron Diffraction. *Acta Crystallogr. Sect. B Struct. Sci. Cryst. Eng. Mater.* **1982**, *38*, 2331–2341. [CrossRef]

51. Angenault, J.; Couturier, J.C.; Souron, J.P.; Siliqi, D.; Quarton, M. The Martensitic Nature of the Transition Monoclinic ⇌ Rhombohedral of $LiSn_2(PO_4)_3$. *J. Mater. Sci. Lett.* **1992**, *11*, 1705–1707. [CrossRef]
52. Altomare, A.; Rizzi, R.; Rossi, M.; El Khouri, A.; Elaatmani, M.; Paterlini, V.; Della Ventura, G.; Capitelli, F. New $Ca_{2.90}(Me^{2+})_{0.10}(PO_4)_2$ β-Tricalcium Phosphates with Me^{2+} = Mn, Ni, Cu: Synthesis, Crystal-Chemistry, and Luminescence Properties. *Crystals* **2019**, *9*, 288. [CrossRef]
53. Capitelli, F.; El Bali, B.; Essehli, R.; Lachkar, M.; da Silva, I. New Hybrid Diphosphates $Ln_2(NH_2(CH_2)_2NH_2)(HP_2O_7)_2 \cdot 4H_2O$(*Ln* = Eu, Tb, Er): Synthesis, Single Crystal and Powder X-Ray Crystal Structure. *Z. Für Krist. Cryst. Mater.* **2006**, *221*, 788–794. [CrossRef]
54. Koutsopoulos, S. Synthesis and Characterization of Hydroxyapatite Crystals: A Review Study on the Analytical Methods. *J. Biomed. Mater. Res.* **2002**, *62*, 600–612. [CrossRef]
55. Jastrzębski, W.; Sitarz, M.; Rokita, M.; Bułat, K. Infrared Spectroscopy of Different Phosphates Structures. *Spectrochim. Acta Part A Mol. Biomol. Spectrosc.* **2011**, *79*, 722–727. [CrossRef]
56. Bulina, N.V.; Chaikina, M.V.; Prosanov, I.Y. Mechanochemical Synthesis of Sr-Substituted Hydroxyapatite. *Inorg. Mater.* **2018**, *54*, 820–825. [CrossRef]
57. Markovic, M.; Fowler, B.O.; Tung, M.S. Preparation and Comprehensive Characterization of a Calcium Hydroxyapatite Reference Material. *J. Res. Natl. Inst. Stand. Technol.* **2004**, *109*, 553. [CrossRef]
58. Jillavenkatesa, A.; Condrate, R.A. The Infrared and Raman Spectra of β-and α-Tricalcium Phosphate ($Ca_3(Po_4)_2$). *Spectrosc. Lett.* **1998**, *31*, 1619–1634. [CrossRef]